Journal of Materials Chemistry A

Bonding Heterogeneity in Mixed-Anion Compounds Realizes Ultralow Lattice Thermal Conductivity

Journal:	*Journal of Materials Chemistry A*
Manuscript ID	TA-ART-06-2021-004958.R1
Article Type:	Paper
Date Submitted by the Author:	08-Sep-2021
Complete List of Authors:	Sato, Naoki; National Institute for Materials Science, International Center for Young Scientists (ICYS); National Institute for Materials Science, International Center for Materials Nanoarchitectonics (WPI-MANA) Kuroda, Norihide; Tokyo Gakugei University Nakamura, Shun; Tokyo Gakugei University Katsura, Yukari; National Institute for Materials Science, Research and Services Division of Materials Data and Integrated System (MaDIS); The University of Tokyo, Department of Advanced Materials Science Kanazawa, Ikuzo; Tokyo Gakugei University Kimura, Kaoru; The University of Tokyo, Department of Advanced Materials Science; National Institute of Advanced Industrial Science and Technology, OPERANDO-OIL Mori, Takao; National Institute for Materials Science, International Center for Materials Nanoarchitectonics (WPI-MANA); University of Tsukuba, Graduate School of Pure and Applied Science

ARTICLE

Bonding Heterogeneity in Mixed-Anion Compounds Realizes Ultralow Lattice Thermal Conductivity†

Naoki Sato,[a,b*] Norihide Kuroda,[c] Shun Nakamura,[c] Yukari Katsura,[d,e] Ikuzo Kanazawa,[c] Kaoru Kimura[e,f] and Takao Mori[b,g]

Received 00th January 20xx,
Accepted 00th January 20xx

DOI: 10.1039/x0xx00000x

Crystalline materials with intrinsically low lattice thermal conductivity (κ_{lat}) pave the way towards high performance in various energy applications, including thermoelectrics. Here we demonstrate a strategy to realize ultralow κ_{lat} using mixed-anion compounds. Our calculations reveal that locally distorted structures in chalcohalides $MnPnS_2Cl$ (Pn = Sb, Bi) derives a bonding heterogeneity, which in turn causes a peak splitting of the phonon density of states. This splitting induces a large amount of scattering phase space. Consequently, κ_{lat} of $MnPnS_2Cl$ is significantly lower than that of a single-anion sulfide $CuTaS_3$ with a similar crystal structure. Experimental κ_{lat} of $MnPnS_2Cl$ takes an ultralow value of about 0.5 W m^{-1} K^{-1} at 300 K. Our findings will encourage the exploration of thermal transport in mixed-anion compounds, which remain a vast unexplored space, especially regarding unexpectedly low κ_{lat} in lightweight materials derived from the bonding heterogeneity.

1. Introduction

Searches for low lattice thermal conductivity (κ_{lat}) materials have been of great importance in achieving high performance in thermoelectrics,[1–3] thermal barrier coatings,[4] and thermal insulation.[5] In the past decade, the validity of some extrinsic effects for reducing κ_{lat}, such as point defects,[6,7] fine grain boundary,[8] nanoscale precipitates,[9] and all-scale hierarchical microstructures,[10] has been successfully demonstrated. However, these strategies usually affect charge carrier mobility, which is detrimental to thermoelectric performance. Thus, understanding the intrinsic mechanisms of thermal transport realizing low κ_{lat} which are associated closely with chemical bonding, crystal structure, and lattice anharmonicity, can be more helpful in some cases, as it provides us with efficient ways to manage both electrical and thermal properties independently.

In recent years, several structural origins bringing intrinsically low κ_{lat} like complex crystal structure,[11–20] resonant bonding,[21–23] stereochemically active lone-pair electrons,[24–31] rattling and its reminiscent anharmonic vibration,[32–41] superionic transition,[42–46] partial occupancy,[47,48] and bonding heterogeneity[27,40,49–57] have been unveiled. Among these, we focus on the bonding heterogeneity, namely the coexistence of strong and weak bonding, as it is more likely to be observed in many classes of crystalline solids and can be utilized more easily to realize low κ_{lat}. The bonding heterogeneity is frequently observed in Zintl phases, which consist of coexisting ionic and covalent sublattices. In addition, local structures containing multiple anions should form a distorted coordination environment, which gives the bonding heterogeneity.

Mixed-anion compounds, solid-state materials containing more than one anionic species in a single phase, have recently attracted much attention because they have potential to offer novel and attractive functionalities which were not observed in conventional "single-anion" materials.[58] Some superior properties in the mixed-anion compounds have already been discovered, such as visible-light photocatalysis, pleochroism, and battery applications.[58] In the thermoelectrics field, anionic solid solutions like PbTe–PbSe[59,60] and Bi_2Te_3–Bi_2Se_3[61] have been regarded as an effective way to realize carrier concentration tuning, band engineering, and reduction of κ_{lat} via phonon-alloy scattering. In addition, a mixed-anion BiCuSeO consisting of $(Cu_2Se_2)^{2-}$ and $(Bi_2O_2)^{2-}$ layers has been a hot material because of its extremely low κ_{lat} and promising figure of merit.[62–64] The origin of low κ_{lat} is derived from large anharmonicity due to the anisotropic layered structure. It is a typical example of mixed-anion compounds containing multiple anions in separate building blocks. On the other hand, the mixed-anion are also likely to form locally distorted structures in which more than one anions are bonded to a cation. This class of materials is less explored in terms of thermal transport.

[a] International Center for Young Scientists (ICYS), National Institute for Materials Science (NIMS), 1-2-1 Sengen, Tsukuba, Ibaraki 305-0047, Japan. E-mail: SATO.Naoki@nims.go.jp
[b] International Center for Materials Nanoarchitectonics (WPI-MANA), NIMS, 1-1 Namiki, Tsukuba, Ibaraki 305-0044, Japan.
[c] Department of Physics, Tokyo Gakugei University, 4-1-1 Nukuikitamachi, Koganei, Tokyo 184-8501, Japan
[d] Research and Services Division of Materials Data and Integrated System (MaDIS), NIMS, 1-1 Namiki, Tsukuba, Ibaraki 305-0047, Japan
[e] Department of Advanced Materials Science, The University of Tokyo, 5-1-5 Kashiwanoha, Kashiwa, Chiba 277-8561, Japan
[f] OPERANDO-OIL, National Institute of Advanced Industrial Science and Technology (AIST), 5-1-5 Kashiwanoha, Kashiwa, Chiba 277-8561, Japan
[g] Graduate School of Pure and Applied Science, University of Tsukuba, 1-1-1 Tennodai, Tsukuba, Ibaraki 305-8671, Japan.
† Electronic Supplementary Information (ESI) available. See DOI: 10.1039/x0xx00000x

Although a few previous reports[52–54,65] deal with this type mixed-anion materials, unique features derived from the mixed-anions are still ambiguous because they are not compared with a single-anion counterpart. We can expect that the locally distorted structures in mixed-anion materials bring the bonding heterogeneity, which effectively realize low κ_{lat}.

Herein, we demonstrate an effective guideline that the mixed-anion framework with distorted local structures is a promising series of materials to realize ultralow κ_{lat}. We chose Mn-based chalcohalides $MnPnS_2Cl$ (Pn = Sb, Bi) as model materials to test the validity of our strategy using mixed-anion compounds. To extract unique features derived from the mixed-anion, a single-anion sulfide $CuTaS_3$, which has some structural similarities to the mixed-anion chalcohalides, was chosen for comparison. By performing calculations based on density functional theory (DFT), we explore lattice dynamics and thermal transport properties of these compounds. We find a remarkable variety of second order interatomic force constants (IFC) within the distorted coordination polyhedra containing multiple anions, which shows significant bonding heterogeneity in this series. Some peak-splitting in the phonon density of states (DOS) originating from the bonding heterogeneity significantly increases the 3-phonon scattering phase space (SPS), which results in a much smaller phonon relaxation time of $MnPnS_2Cl$ than $CuTaS_3$. Consequently, the calculated κ_{lat} of $MnPnS_2Cl$ is strikingly about seven times lower than $CuTaS_3$. The synthesized polycrystalline sample of $MnPnS_2Cl$ is actually demonstrated to exhibit the ultralow κ_{lat} of about 0.5 W m^{-1} K^{-1} at room temperature. Considering the relatively low density and averaged atomic mass of $MnSbS_2Cl$, this mixed-anion approach can give a route to uncover lightweight materials with low κ_{lat}.

2. Results and Discussion

The crystal structures of mixed-anion chalcohalides $MnPnCh_2X$ (Pn = Sb, Bi, Ch = S, Se, X = Cl, Br, I) series, including our target materials, were originally investigated by single-crystal X-ray and neutron diffraction.[66–68] Fig. 1a shows the crystal structure of the mixed-anion chalcohalides visualized by VESTA 3.[69] $MnSbS_2Cl$ and $MnBiS_2Cl$ crystallize in the orthorhombic structure (space group *Pnma*).[66,67] The primitive cell contains five crystallographically inequivalent atoms, Mn, Sb/Bi, S(1), S(2), and Cl. All the atoms occupy 4c Wyckoff position. These compounds are composed of locally distorted structures derived from constituent multiple anions. The coordination environments around Mn and Sb/Bi atoms are shown in Fig. 1b and 1c, respectively. The Mn atom is octahedrally coordinated by four S and two Cl atoms with *cis*-geometry. The Sb/Bi atom is coordinated by five S and three Cl atoms. The interatomic distances between Sb/Bi and Cl are much longer than those between Sb/Bi and S atoms. These polyhedra share their edges and vertices and form infinite chains along the *b*-axis. The locally distorted structures containing different bond lengths and chemical environments should result in a significant bonding heterogeneity, which in turn can cause interesting lattice dynamics and thermal transport properties. It is necessary to make a comparison between the mixed-anion compounds and a single-anion counterpart which resembles each other, in order to extract unique features originating from the mixed-anion state. $CuTaS_3$, a single-anion sulfide, has some structural similarity to $MnPnS_2Cl$. Fig. 1d shows the crystal structure of $CuTaS_3$. $CuTaS_3$ crystallizes in the orthorhombic structure with space group *Pnma*, and the primitive cell contains five crystallographically inequivalent atoms, Cu, Ta, S(1), S(2), and S(3).[70] All the atoms occupy 4c Wyckoff position. The coordination environments around Cu and Ta atoms are shown in Fig. 1e and 1f, respectively. In the ICSD database, $MnPnCh_2X$ is classified as the same structure-type as $CuTaS_3$ though the local structures are quite different. The Cu atom is tetrahedrally

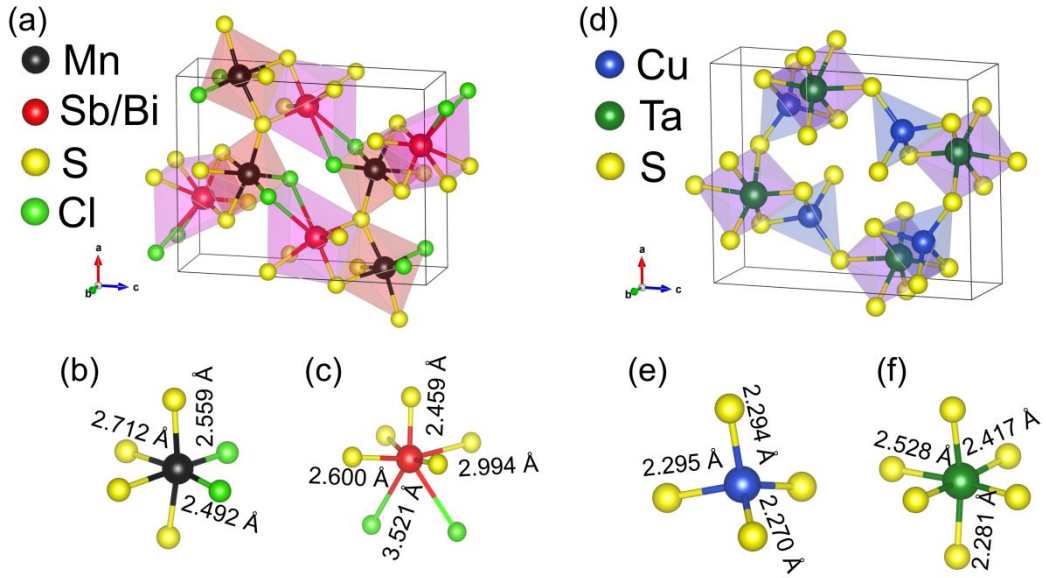

Fig. 1 (a) The unit cells of $MnPnS_2Cl$ (Pn =Sb, Bi) and the coordination environments around (b) Mn and (c) Sb/Bi atoms. (d) The unit cell of $CuTaS_3$ and the coordination environment around (e) Cu and (f) Ta atoms. The interatomic distances of atom pairs are shown along each bond. The value shown in (b) and (c) correspond to $MnSbS_2Cl$.

ARTICLE

coordinated by four S atoms, and the Ta atom is octahedrally coordinated by six S atoms. The bond lengths within the coordination polyhedra vary despite the single anion, but to a lesser extent than the mixed-anion $MnPnS_2Cl$. In addition, $MnBiS_2Cl$ and $CuTaS_3$ have the similar theoretical density of 5.32 g cm^{-3} and 5.82 g cm^{-3}, respectively, and the same percentage of heavy atoms where 20% of the constituent elements are heavy (Sb, Bi, Ta) and 80% are relatively light (Mn, Cu, S, Cl). Thus, $CuTaS_3$ is a suitable material to compare the lattice dynamics with $MnPnS_2Cl$ to gain insight into the crucial roles of the mixed-anion.

We performed DFT-based calculations to investigate lattice dynamics and thermal transport properties of the mixed-anion $MnPnS_2Cl$ and the single-anion $CuTaS_3$. Fig. 2 shows the norm of calculated second-order IFC matrix, $|\Phi^{ij}|$ as a function of interatomic distance. The IFC represents the strength of interaction between each atomic pair, namely bond strength. The IFCs decay rapidly with increasing interatomic distance though some non-negligible components are observed for Sb-S, Bi-S, and Ta-S bonds at around 6 Å. The IFCs of Cu-S bonds in the coordination tetrahedron of $CuTaS_3$ with almost identical bond length range from 4 to 5 eV Å^{-2}, while those of Ta-S bonds range from 4 to 7 eV Å^{-2} due to slightly different bond length and distorted coordination. On the other hand, the IFCs of the nearest and second nearest Mn-S and Mn-Cl differ by a factor of about 3–6. For the nearest Sb-S (Bi-S) and Sb-Cl (Bi-Cl), the IFCs differ by a factor of 23 (18). These indicate that the local structures in the mixed-anion $MnPnS_2Cl$ hold the remarkable bonding heterogeneity compared to $CuTaS_3$. This significant difference of bonding environment between the mixed- and single-anion compounds can cause interesting features in lattice dynamics. To gain further insight into the electronic origin of the bonding heterogeneity, we examined the charge density and electron localization function (ELF), as shown in Fig. S1 in the Supplementary Information. The Mn-S shows a bit more covalency than the Mn-Cl bond both in $MnSbS_2Cl$ and $MnBiS_2Cl$. This behavior can be understood by the larger electronegativity of Cl than S. The bonding environment surrounding Sb in $MnSbS_2Cl$ and Bi in $MnBiS_2Cl$ looks different. The Sb-S exhibits covalency while the valence electrons of Sb in the Sb-Cl direction are strongly localized according to ELF. On the other hand, in $MnBiS_2Cl$, the electrons surrounding Cl in the Bi-Cl direction are localized instead of Bi. However, both bonding character results in the bonding heterogeneity, namely the significant difference in the IFC between Pn-S and Pn-Cl bonding.

The calculated phonon dispersion curves together with the phonon DOS are shown in Fig. 3a, 3b, and 3c. These compounds are dynamically stable as no imaginary modes are observed in the phonon dispersion. As shown in the atom-decomposed phonon DOS, the acoustic modes mainly originate from the heaviest atom (Sb, Bi, and Ta for $MnSbS_2Cl$, $MnBiS_2Cl$, and $CuTaS_3$, respectively). For $CuTaS_3$, high-frequency optical modes (> 250 cm^{-1}) mainly derive from S atom, while heavier Cu and Ta atoms mainly contribute to the lower modes (< 180 cm^{-1}). As a result, a gap-like opened structure is observed in the phonon DOS at around 180–250 cm^{-1}. On the other hand, the gap-like structure is not observed in the phonon DOS of $MnPnS_2Cl$. For $MnPnS_2Cl$, high-frequency region (> 200 cm^{-1}) is like $CuTaS_3$, namely large contribution from S atom. However, Cl atom contributes to the lower frequency region (70–200 cm^{-1}) despite its almost the same atomic mass as S (S: 32.07 g mol^{-1}, Cl: 35.45 g mol^{-1}). This splitting of the peak in the phonon DOS between S and Cl is derived from the bonding heterogeneity. The phonon frequency ω is related to the atomic mass and the second-order IFC:

$$\omega^2 \propto \frac{1}{\sqrt{M_A M_B}} \sum \Phi \quad (1)$$

where M_A and M_B are the atomic mass of species A and B, respectively, and Φ is the second-order IFC. Thus, a significant variety of the IFC originating from the bonding heterogeneity results in the splitting of phonon frequency, even though the atomic mass of multiple anions is almost the same. Fig. 3d shows a schematic diagram representing the situation occurred

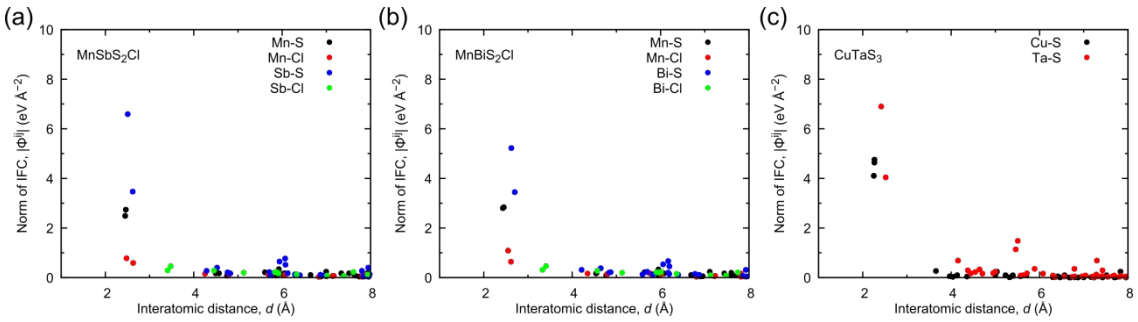

Fig. 2 Norm of IFC matrix, $|\Phi^{ij}|$, as a function of interatomic distance between atoms denoted by *i* and *j* for (a) $MnSbS_2Cl$, (b) $MnBiS_2Cl$, and (c) $CuTaS_3$.

ARTICLE

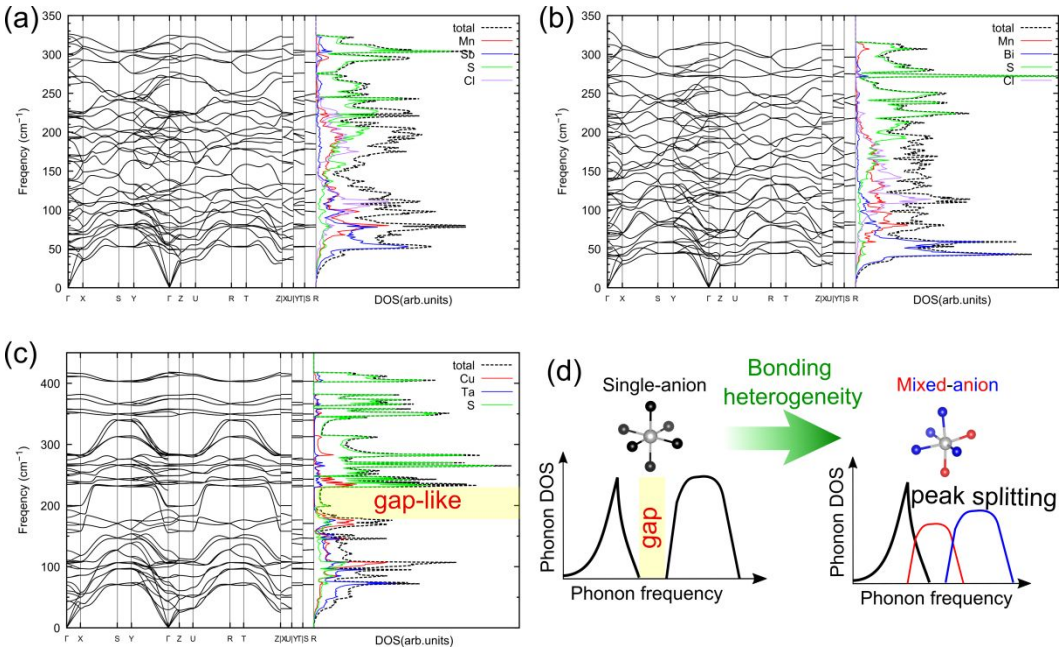

Fig. 3 The calculated phonon dispersion and the total and atom-decomposed phonon DOS for (a) $MnSbS_2Cl$, (b) $MnBiS_2Cl$, and (c) $CuTaS_3$. A colored region in (c) represents a gap-like opened structure observed in the phonon DOS of $CuTaS_3$. (d) A schematic diagram representing the change of phonon DOS from single-anion to mixed-anion materials induced by the bonding heterogeneity. The gap-like structure of DOS observed in the single-anion is filled with additional states formed by peak splitting in the mixed-anion one.

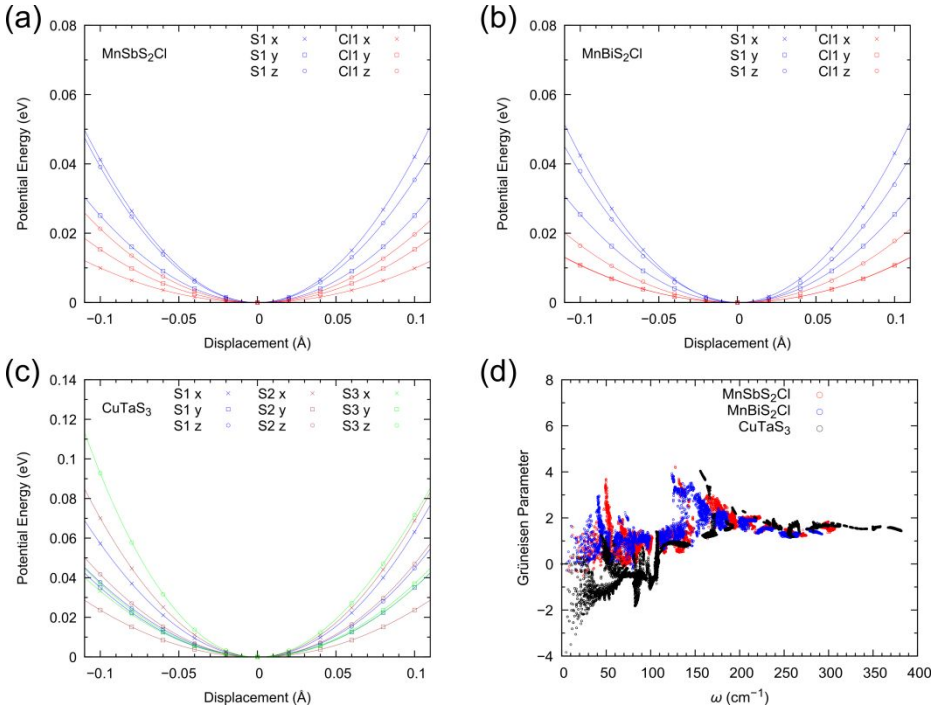

Fig. 4 The calculated potential energy of each atomic site as a function of displacements along cartesian *x*-, *y*-, and *z*-directions for (a) $MnSbS_2Cl$, (b) $MnBiS_2Cl$, and (c) $CuTaS_3$. Solid lines are fitting curves using up to cubic term. (d) The calculated Grüneisen parameter as a function of the phonon frequency.

ARTICLE

here. The gap-like structure observed in the phonon DOS of the single-anion material is filled with additional states generated from the peak splitting induced by the bonding heterogeneity in the mixed-anion material with locally distorted structures.

A potential energy surface that provides us with insight into anharmonicity at each atomic site can be visualized by plotting an energy change with respect to a displacement of the atom. Fig. 4a, 4b, and 4c show the potential energy of anion sites as a function of displacements along cartesian *x*-, *y*-, and *z*-directions for $MnSbS_2Cl$, $MnBiS_2Cl$, and $CuTaS_3$, respectively, with fitting curves using up to cubic term. The fitting using only quadratic term is shown in Fig. S2 in the Supplementary Information. The potential energy of all sites, including cation sites, is shown in Fig. S3 in the Supplementary Information. The anions in $MnPnS_2Cl$ lie in almost harmonic potential while S3 site in $CuTaS_3$ deviates from harmonic behavior signigicantly. As shown in Fig. S3, cation sites both for $MnPnS_2Cl$ and $CuTaS_3$ exhibit more asymmetric and anharmonic features than anions. The Cl atoms of $MnPnS_2Cl$ lie in a flatter potential than the S atoms, which is consistent with the weaker bonding environment and the lower phonon frequency of the Cl atoms. The difference in anisotropy of potential surrounding Cl atoms between $MnSbS_2Cl$ and $MnBiS_2Cl$, namely the shallower potential in the *y*-direction for $MnBiS_2Cl$, can be derived from the difference in the Mn-Cl bond length (2.492 Å in $MnSbS_2Cl$ and 2.549 Å in $MnBiS_2Cl$). The shallow potential well also corresponds to the large thermal displacement parameters represented by the mean square displacement, as shown in Fig. S4 in the Supplementary Information. To further gain insight into the anharmonicity of these compounds, we calculated the Grüneisen parameters as shown in Fig. 4d. The Grüneisen parameter is defined by the change of phonon frequency with respect to the change of volume of the unit cell. Some compounds possessing lone-pair electrons and low κ_{lat} show anomalously large Grüneisen parameter exceeding 50.[24,27] For the low frequency region of acoustic modes, the magnitude of the Grüneisen parameter is larger for $CuTaS_3$ than $MnPnS_2Cl$ while $MnPnS_2Cl$ has larger values at around 50 cm^{-1} and 150 cm^{-1}. From the Grüneisen parameter, we can see that both $MnPnS_2Cl$ and $CuTaS_3$ has moderate anharmonicity compared to extremely anharmonic materials.[24,27]

To achieve further insight into the relationship between the bonding heterogeneity and the thermal transport, we calculated the 3-phonon SPS. The SPS is a measure of the amount of available scattering processes satisfying the energy and momentum conservation. The SPS is given as

$$W_q^{\pm} = \frac{1}{N}\sum_{q',q''}\begin{Bmatrix} n_{q''}-n_{q'} \\ n_{q'}+n_{q''}+1 \end{Bmatrix}\delta(\omega_q - \omega_{q'} \pm \omega_{q''}) \quad (2)$$

where W_q^+ and W_q^- are the SPS corresponding to absorption and emission processes of phonon mode q, respectively. Here, the variable q is defined by $q = (\boldsymbol{q}, j)$ and $-q = (-\boldsymbol{q}, j)$ where $\boldsymbol{q}$ and j are the wave vector and the branch index of phonon modes. n_q is the Bose-Einstein distribution function. Fig. 5a and 5b show W_q^+ and W_q^- as a function of the phonon freuquency at 300 K, respectively. Notably, W_q^+ at the low-frequency region and W_q^- at the middle and high-frequency region are several

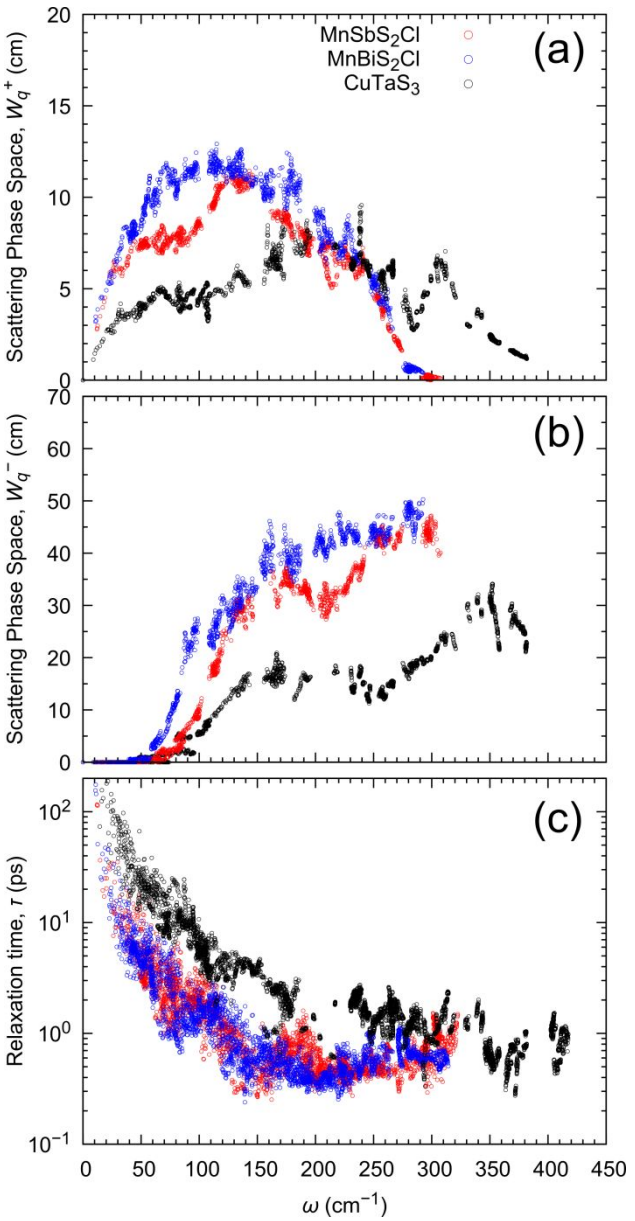

Fig. 5 The calculated 3-phonon SPS for (a) absorption and (b) emission processes, and (c) 3-phonon relaxation time at 300 K as a function of the phonon frequency.

ARTICLE

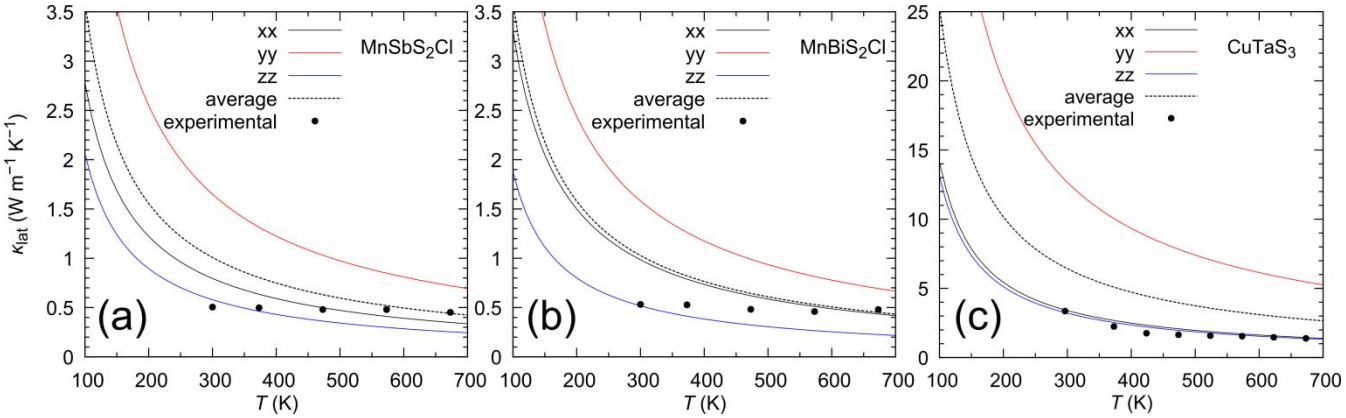

Fig. 6 The temperature dependence of calculated and experimental κ_{lat} for (a) $MnSbS_2Cl$, (b) $MnBiS_2Cl$, and (c) $CuTaS_3$.

times larger for $MnPnS_2Cl$ than $CuTaS_3$. These differences should originate from the peak splitting of phonon DOS discussed above, as represented by Fig. 3d. The gap-like structure observed in the phonon DOS causes the lower amount of 3-phonon scattering processes between acoustic-optical and optical-optical modes. The gap is filled with the additional states induced by the bonding heterogeneity, which results in the increase of acoustic-optical and optical-optical scattering processes. The SPS is proportional to the 3-phonon scattering rate, the inverse of phonon relaxation time τ. In other words, the larger the SPS, the smaller the τ. Thus, the larger SPS brings the lower κ_{lat}. Fig. 5c shows the 3-phonon relaxation time as a function of the phonon frequency at 300 K. At the overall frequency range, the τ of $MnPnS_2Cl$ is significantly smaller than that of $CuTaS_3$. As shown in Fig. S5 in the Supplementary Information, the phonon group velocity of acoustic modes of $MnPnS_2Cl$ and $CuTaS_3$ is not essentially different, while the optical modes of $CuTaS_3$ at around 150–250 cm^{-1}, corresponding to the dispersive curve in Fig. 3c, have much larger value. However, this large group velocity of the optical modes of $CuTaS_3$ has a negligible contribution to the lattice thermal conductivity, as shown in the spectral thermal conductivity (Fig. S6, Supplementary Information). Also, the difference in the highest value of phonon frequency (~330 cm^{-1} for $MnPnS_2Cl$ and ~420 cm^{-1} for $CuTaS_3$) is not significantly relevant for κ_{lat} because the contribution of high-frequency optical modes above 300 cm^{-1} to the thermal conductivity can be negligible. Therefore, the significant difference in the τ between $MnPnS_2Cl$ and $CuTaS_3$ is a dominant factor determining the difference in κ_{lat}.

We calculated the κ_{lat} by solving the phonon Boltzmann transport equation within the single mode relaxation time approximation. The calculation only considers the intrinsic 3-phonon scattering. Fig. 6a, 6b, and 6c show the temperature dependence of the κ_{lat} (*xx*, *yy*, and *zz* components) for $MnSbS_2Cl$, $MnBiS_2Cl$, and $CuTaS_3$, respectively. The averaged value of each direction is also shown. In addition, we synthesized the polycrystalline samples of $MnSbS_2Cl$, $MnBiS_2Cl$, and $CuTaS_3$ by solid-state reaction, melting, and spark plasma sintering and measured the experimental κ_{lat} (see Experimental Procedure and measured X-ray diffraction patterns in Fig. S7 in the Supplementary Information). The sintered samples of $MnPnS_2Cl$ contain a tiny amount of unknown impurity phases. We can regard the impurity phases to have little effects on the transport properties above room temperature. The temperature dependence of the experimental κ_{lat} is plotted in Fig. 6a, 6b, and 6c. The calculated κ_{lat} shows a significant anisotropy for these compounds due to the anisotropic crystal structures. The

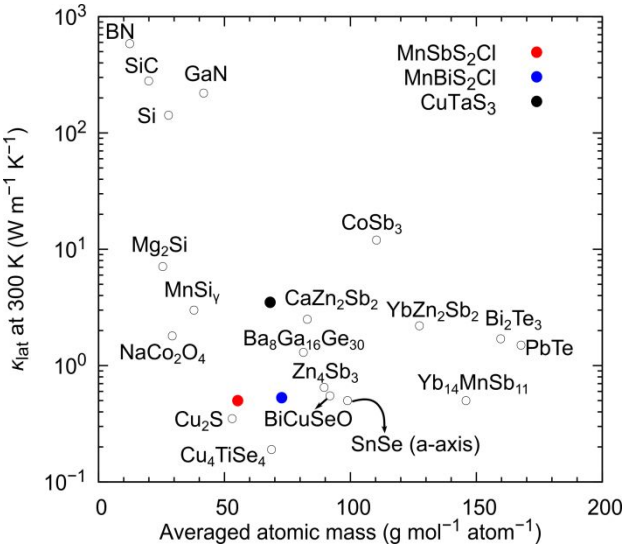

Fig. 7 κ_{lat} at 300 K versus averaged atomic mass for various compounds including the mixed-anion $MnPnS_2Cl$ (this work), $CuTaS_3$ (this work), h-BN (in-plane),[77] 4H-SiC,[78] Si,[79]

GaN,[80] Mg_2Si,[81] $CoSb_3$,[82] Bi_2Te_3,[83] PbTe,[84] $Yb_{14}MnSb_{11}$,[85] $YbZn_2Sb_2$,[85] $CaZn_2Sb_2$,[85] Zn_4Sb_3,[86] $MnSi_\gamma$,[14] Cu_2S,[46] $Ba_8Ga_{16}Ge_{30}$,[36] BiCuSeO,[62] SnSe (*a*-axis),[87] $NaCo_2O_4$,[88] and Cu_4TiSe_4.[89]

averaged calculated values at 300 K are 1.1 W m^{-1} K^{-1}, 1.0 W m^{-1} K^{-1}, and 7.2 W m^{-1} K^{-1} for $MnSbS_2Cl$, $MnBiS_2Cl$, and $CuTaS_3$, respectively. The temperature dependence of the experimental κ_{lat} for $MnPnS_2Cl$ is flat, while the calculated one obeys T^{-1} dependence. The experimental values at 300 K are 0.50 W m^{-1} K^{-1}, 0.53 W m^{-1} K^{-1}, and 3.5 W m^{-1} K^{-1}, respectively. Both the calculated and experimental values differ strikingly by a factor of 7 between $MnPnS_2Cl$ and $CuTaS_3$. The deviation between the absolute values of calculated and experimental κ_{lat} can be due to several factors: the experimental κ_{lat} contains the effect of grain boundary and chemical disorder. Moreover, some effects unveiled in recent years are beyond the scope of our calculations, such as the temperature dependent anharmonicity[71] and crystal/amorphous boundary behavior,[72,73] which might contribute to the glass-like flat temperature dependence.

It is worth mentioning again that the significantly lower κ_{lat} of $MnPnS_2Cl$ than $CuTaS_3$ is mainly due to the enhanced SPS, which is harmonic vibrational property. The Grüneisen parameter suggests no significant difference in the lattice anharmonicity, which is closely connected to the strength of each 3-phonon scattering process.[74] There are some other known systems in which the SPS is a good measure of κ_{lat}.[75,76]

We have discovered that the mixed-anion $MnPnS_2Cl$ exhibits the ultralow κ_{lat} even at room temperature. Considering the relatively low density ($MnSbS_2Cl$: 4.12 g cm^{-3}, $MnBiS_2Cl$: 5.32 g cm^{-3}) and averaged atomic mass per atom ($MnSbS_2Cl$: 55.27 g mol^{-1} $atom^{-1}$, $MnBiS_2Cl$: 72.71 g mol^{-1} $atom^{-1}$), the κ_{lat} values of these compounds are unexpectedly low. Light atoms generally make stronger and more covalent bonding than heavier ones, which typically leads to high κ_{lat}. To highlight the anomaly of the mixed-anion compounds, we plotted the κ_{lat} versus the averaged atomic mass of various materials, including simple semiconductors and some known thermoelectric materials with low κ_{lat} in Fig. 7. Almost all materials with κ_{lat} < 1 W m^{-1} K^{-1} shown here have large averaged atomic mass larger than 80 g mol^{-1} $atom^{-1}$, except for $MnPnS_2Cl$, Cu_2S,[46] and Cu_4TiSe_4.[89] Cu_2S undergoes two phase transitions and possesses liquid-like copper ions, which results in ultralow κ_{lat}.[46] The extremely low κ_{lat} of Cu_4TiSe_4, 0.19 W m^{-1} K^{-1} at 300 K, was very recently confirmed and attributed to its highly disordered structure and soft phonon modes.[89] Note that the lightweight and ultralow κ_{lat} $MnPnS_2Cl$ contains none of the phase transitions, structural instability, and extremely high anharmonicity but contains the bonding heterogeneity induced by the locally distorted structures.

A great advantage of the bonding heterogeneity by mixed-anion concept to realize low κ_{lat}, summarized in Fig. 3d, is that the phonon frequency of light atoms, like Cl in this work, can be lowered so that the number of optical modes whose frequency are close to acoustic modes increases. It means that the strategy can be utilized to explore lightweight and low κ_{lat} materials. In particular, abundant mixed-anion materials unknown in terms of thermal conductivity, such as oxynitrides, oxysulfides, and chalcohalides, can be promising candidates.

3. Conclusions

In conclusion, we have demonstrated that the locally distorted structures observed in the mixed-anion compounds derive ultralow κ_{lat}. Using DFT-based calculations, we clarified the significant variety of the second-order IFC in the mixed-anion $MnPnS_2Cl$, which represents the bonding heterogeneity. This bonding environment causes the remarkable splitting of the phonon frequency, which essentially increases the amount of 3-phonon scattering processes. The increased SPS leads to the lower phonon relaxation time. Consequently, κ_{lat} of $MnPnS_2Cl$ is significantly lower than that of a single-anion sulfide $CuTaS_3$ with the similar crystal structure and percentage of heavy atoms. Experimental κ_{lat} of $MnPnS_2Cl$ shows an ultralow value of about 0.5 W m^{-1} K^{-1} at room temperature, which is unexpectedly low considering the relatively low averaged atomic mass per atom of these compounds. A possible future work will be to confirm whether the strategy found in this work can be applied to a broader range of the mixed-anion compounds. Our study decorates the mixed-anion compounds, which remain a vast unexplored space, with novel thermal functionality.

4 Experimental Section

Synthesis

Polycrystalline samples of $MnPnS_2Cl$ were synthesized by solid state reaction of stoichiometric amounts of MnS, $MnCl_2$, and Pn_2S_3 (1:1:1). The starting materials were weighed and ground with an agate mortar in an Ar-filled glovebox, and then transferred to quartz tubes and sealed under a high vacuum. These ampoules were put into a box furnace and heated to 773 K for 2 hours, and kept for 7 days. The obtained ingots were ground into fine powders (< 45 μm) and consolidated by spark plasma sintering (SPS, SPS-515S, Fuji Electronic Industrial Co., Japan). To obtain dense and high-purity bulk samples, we applied high-pressure and low-temperature conditions for SPS. The powder samples were set in a 10 mm diameter cemented carbide die, heated to 813 K with a uniaxial pressure of 500 MPa under Ar atmosphere, and then held for 30 min. The dense bulk samples with relative density ~98% were obtained.

A polycrystalline sample of $CuTaS_3$ was synthesized by melting and following solid state reaction of element powders Cu, Ta, and S. To avoid S-poor impurity phases, the nominal composition was set to $CuTaS_{3.2}$. The starting materials were weighed and ground with the agate mortar, and then transferred to a quartz tube and sealed under a high vacuum. The ampoule was put into the box furnace and heated to 923 K for 24 hours, and kept for 7 days. The obtained ingot was ground into fine powders (< 45 μm) and consolidated by SPS. The powder sample was set in a 10 mm diameter graphite die, heated to 873 K with a uniaxial pressure of 100 MPa under Ar

atmosphere, and then held for 10 min. The dense bulk sample with relative density ~98% was obtained.

Characterization

The phase identification of the samples was performed by X-ray diffraction (XRD) measurements using Cu K_α radiation (SmartLab, Rigaku Co., Japan). The thermal conductivity κ was brought by $\kappa = DC_pd$, where D, C_p, and d are the thermal diffusivity, the specific heat, and the density, respectively. The thermal diffusivity and the specific heat were concurrently measured for the disk-shaped samples by laser flash method (LFA 467 Hyperflash, Netzsch, Germany) with a pyroceram disk as a reference sample. The sample density was measured by Archimedes method. The lattice thermal conductivity κ_{lat} can be regarded as the same as the measured κ because $MnPnS_2Cl$ and $CuTaS_3$ are insulators with high electrical resistivity.

Computational Method

We performed *ab initio* calculations based on density functional theory (DFT). The Quantum Espresso (QE) package[90,91] with projector-augmented wave pseudopotentials[92,93] was used for total energy calculations. The generalized gradient approximation functional with Perdew–Burke–Ernzerhof parametrization revised for solids (GGA-PBEsol)[94] was employed for the exchange and correlation potentials. For $MnPnS_2Cl$ (Pn = Sb, Bi), we employed spin-polarized settings with oppositely oriented magnetic moments on Mn atoms. Initial values of magnetic moments of Mn atoms were set to ±5 μ_B, and after structure relaxation, they were converged to ±4.19 μ_B and ±4.15 μ_B for $MnSbS_2Cl$ and $MnBiS_2Cl$, respectively. *k*-point grids of 6 × 14 × 4 and 6 × 15 × 4 and energy cutoff of 100 Ry and 90 Ry for the primitive cell of $MnPnS_2Cl$ and $CuTaS_3$, respectively, were used for structure relaxation. The lattice parameters of the relaxed primitive cell of $MnPnS_2Cl$ and $CuTaS_3$ are listed in Table S1.

To extract the second and third order interatomic force constants (IFC), we used finite difference method with 2 × 3 × 1 supercells containing 120 atoms based on the fully relaxed primitive cell to create displacement-force datasets. The magnitude of atomic displacements was set at 0.01 Å and 0.04 Å for calculating the second and third order IFCs, respectively. For the third order IFC calculation, we chose the cutoff radius as 14.2 Å for choosing triplets within which interaction is considered. The IFCs were obtained using ALAMODE[95] code. The phonon dispersion relation and density of states (DOS) were calculated from the second order IFC. The sampling grids used for summation were 7 × 17 × 5 and 7 × 18 × 6 for $MnPnS_2Cl$ and $CuTaS_3$, respectively. Dielectric constant and Born effective charge were calculated in the perturbation framework implemented in the QE package for correcting phonon frequencies considering long-range interaction. ALAMODE code is also used to calculate the lattice thermal conductivity by solving the phonon Boltzmann transport equation within the single mode relaxation time approximation. The sampling grids 7 × 17 × 5 and 7 × 18 × 6 for $MnSbS_2Cl$ and $MnBiS_2Cl$, respectively, were applied after confirming convergence of the calculated lattice thermal conductivity with respect to the grid density.

Author Contributions

Naoki Sato: conceptualization, data curation, formal analysis, investigation, methodology, project administration, software, validation, visualization, writing – original draft, writing – review & editing. Norihide Kuroda: investigation. Shun Nakamura: investigation. Yukari Katsura: supervision. Ikuzo Kanazawa: supervision. Kaoru Kimura: supervision, writing – review & editing. Takao Mori: funding acquisition, project administration, supervision, writing – review & editing.

Conflicts of interest

There are no conflicts to declare.

Acknowledgements

This work was supported by the JSPS JP16H06441, JP17H02749, and JST Mirai Program JPMJMI19A1, CREST JPMJCR19Q4. The computation in this work has been performed using the Numerical Materials Simulator at NIMS and SGI Rackable C2112-4GP3/C1102-GP8 (Reedbush-U/H/L) in the Information Technology Center, The University of Tokyo.

References

1 J. Mao, Z. Liu, J. Zhou, H. Zhu, Q. Zhang, G. Chen and Z. Ren, *Adv. Phys.*, 2018, **67**, 69–147.
2 T. Mori, *Small*, 2017, **13**, 1702013.
3 N. Nandihalli, C.-J. Liu and T. Mori, *Nano Energy*, 2020, **78**, 105186.
4 R. Vaßen, M. O. Jarligo, T. Steinke, D. E. Mack and D. Stöver, *Surf. Coatings Technol.*, 2010, **205**, 938–942.
5 D. M. Smith, A. Maskara and U. Boes, *J. Non. Cryst. Solids*, 1998, **225**, 254–259.
6 L. Hu, T. Zhu, X. Liu and X. Zhao, *Adv. Funct. Mater.*, 2014, **24**, 5211–5218.
7 Y. Cao, X. Su, F. Meng, T. P. Bailey, J. Zhao, H. Xie, J. He, C. Uher and X. Tang, *Adv. Funct. Mater.*, 2020, **30**, 2005861.
8 B. Poudel, Q. Hao, Y. Ma, Y. Lan, A. Minnich, B. Yu, X. Yan, D. Wang, A. Muto, D. Vashaee, X. Chen, J. Liu, M. S. Dresselhaus, G. Chen and Z. Ren, *Science (80-.).*, 2008, **320**, 634–638.
9 S. H. Lo, J. He, K. Biswas, M. G. Kanatzidis and V. P. Dravid, *Adv. Funct. Mater.*, 2012, **22**, 5175–5184.
10 K. Biswas, J. He, I. D. Blum, C.-I. Wu, T. P. Hogan, D. N. Seidman, V. P. Dravid and M. G. Kanatzidis, *Nature*, 2012, **489**, 414–418.
11 N. Sato, H. Ouchi, Y. Takagiwa and K. Kimura, *Chem. Mater.*, 2016, **28**, 529–533.
12 Y. Iwasaki, K. Kitahara and K. Kimura, *Phys. Rev. Mater.*, 2019, **3**, 061601.
13 Y. Miyazaki, D. Igarashi, K. Hayashi, T. Kajitani and K. Yubuta, *Phys. Rev. B*, 2008, **78**, 214104.
14 Y. Miyazaki, H. Hamada, H. Nagai and K. Hayashi, *Materials (Basel).*, 2018, **11**, 926.
15 T. Takeuchi, *Zeitschrift für Krist. - Cryst. Mater.*, 2009, **224**, 35–38.

16 K. Tobita, N. Sato, K. Kitahara, Y. Takagiwa and K. Kimura, *Mater. Trans.*, 2016, **57**, 1045–1049.
17 W. Li, J. Carrete, G. K. H. Madsen and N. Mingo, *Phys. Rev. B*, 2016, **93**, 205203.
18 G. A. Slack, in *Semiconductors and Semimetals*, eds. F. Seitz, D. Turnbull and H. Ehrenreich, Academic Press, New York, 34th edn., 1979, p. 1.
19 T. Mori, *J. Solid State Chem.*, 2019, **275**, 70–82.
20 Y. Kakefuda, K. Yubuta, T. Shishido, A. Yoshikawa, S. Okada, H. Ogino, N. Kawamoto, T. Baba and T. Mori, *APL Mater.*, 2017, **5**, 126103.
21 S. Lee, K. Esfarjani, T. Luo, J. Zhou, Z. Tian and G. Chen, *Nat. Commun.*, 2014, **5**, 3525.
22 S. Maier, S. Ohno, G. Yu, S. D. Kang, T. C. Chasapis, V. A. Ha, S. A. Miller, D. Berthebaud, M. G. Kanatzidis, G.-M. Rignanese, G. Hautier, G. J. Snyder and F. Gascoin, *Chem. Mater.*, 2018, **30**, 174–184.
23 W. Zhang, N. Sato, K. Tobita, K. Kimura and T. Mori, *Chem. Mater.*, 2020, **32**, 5335–5342.
24 M. D. Nielsen, V. Ozolins and J. P. Heremans, *Energy Environ. Sci.*, 2013, **6**, 570–578.
25 Y. Dong, A. R. Khabibullin, K. Wei, J. R. Salvador, G. S. Nolas and L. M. Woods, *ChemPhysChem*, 2015, **16**, 3264–3270.
26 M. Dutta, K. Pal, U. V. Waghmare and K. Biswas, *Chem. Sci.*, 2019, **10**, 4905–4913.
27 K. Pal, J. He and C. Wolverton, *Chem. Mater.*, 2018, **30**, 7760–7768.
28 M. Dutta, M. Samanta, T. Ghosh, D. J. Voneshen and K. Biswas, *Angew. Chemie Int. Ed.*, 2021, **60**, 4259–4265.
29 P. Acharyya, T. Ghosh, K. Pal, K. Kundu, K. Singh Rana, J. Pandey, A. Soni, U. V. Waghmare and K. Biswas, *J. Am. Chem. Soc.*, 2020, **142**, 15595–15603.
30 M. K. Jana, K. Pal, U. V. Waghmare and K. Biswas, *Angew. Chemie Int. Ed.*, 2016, **55**, 7792–7796.
31 B. Du, K. Chen, H. Yan and M. J. Reece, *Scr. Mater.*, 2016, **111**, 49–53.
32 G. S. Nolas, D. T. Morelli and T. M. Tritt, *Annu. Rev. Mater. Sci.*, 1999, **29**, 89–116.
33 Y. Zhu, Z. Han, F. Jiang, E. Dong, B.-P. Zhang, W. Zhang and W. Liu, *Mater. Today Phys.*, 2021, **16**, 100327.
34 S. O. Long, A. V. Powell, S. Hull, F. Orlandi, C. C. Tang, A. R. Supka, M. Fornari and P. Vaqueiro, *Adv. Funct. Mater.*, 2020, **30**, 1909409.
35 Z. Liu, N. Sato, W. Gao, K. Yubuta, N. Kawamoto, M. Mitome, K. Kurashima, Y. Owada, K. Nagase, C.-H. Lee, J. Yi, K. Tsuchiya and T. Mori, *Joule*, 2021, **5**, 1196–1208.
36 T. Takabatake, K. Suekuni, T. Nakayama and E. Kaneshita, *Rev. Mod. Phys.*, 2014, **86**, 669–716.
37 K. Suekuni, C. H. Lee, H. I. Tanaka, E. Nishibori, A. Nakamura, H. Kasai, H. Mori, H. Usui, M. Ochi, T. Hasegawa, M. Nakamura, S. Ohira-Kawamura, T. Kikuchi, K. Kaneko, H. Nishiate, K. Hashikuni, Y. Kosaka, K. Kuroki and T. Takabatake, *Adv. Mater.*, 2018, **30**, 1706230.
38 M. K. Jana, K. Pal, A. Warankar, P. Mandal, U. V Waghmare and K. Biswas, *J. Am. Chem. Soc.*, 2017, **139**, 4350–4353.
39 M. Dutta, S. Matteppanavar, M. V. D. Prasad, J. Pandey, A. Warankar, P. Mandal, A. Soni, U. V. Waghmare and K. Biswas, *J. Am. Chem. Soc.*, 2019, **141**, 20293–20299.
40 K. Pal, Y. Xia, J. He and C. Wolverton, *Phys. Rev. Mater.*, 2019, **3**, 085402.
41 H. Lin, G. Tan, J.-N. Shen, S. Hao, L.-M. Wu, N. Calta, C. Malliakas, S. Wang, C. Uher, C. Wolverton and M. G. Kanatzidis, *Angew. Chemie Int. Ed.*, 2016, **55**, 11431–11436.
42 H. Liu, X. Shi, F. Xu, L. Zhang, W. Zhang, L. Chen, Q. Li, C. Uher, T. Day and G. J. Snyder, *Nat. Mater.*, 2012, **11**, 422–425.
43 L. Li, Y. Liu, J. Dai, A. Hong, M. Zeng, Z. Yan, J. Xu, D. Zhang, D. Shan, S. Liu, Z. Ren and J.-M. Liu, *J. Mater. Chem. C*, 2016, **4**, 5806–5813.
44 S. Roychowdhury, M. K. Jana, J. Pan, S. N. Guin, D. Sanyal, U. V. Waghmare and K. Biswas, *Angew. Chemie Int. Ed.*, 2018, **57**, 4043–4047.
45 J. Ding, J. L. Niedziela, D. Bansal, J. Wang, X. He, A. F. May, G. Ehlers, D. L. Abernathy, A. Said, A. Alatas, Y. Ren, G. Arya and O. Delaire, *Proc. Natl. Acad. Sci.*, 2020, **117**, 3930–3937.
46 Y. He, T. Day, T. Zhang, H. Liu, X. Shi, L. Chen and G. J. Snyder, *Adv. Mater.*, 2014, **26**, 3974–3978.
47 T. Mori, J. Martin and G. Nolas, *J. Appl. Phys.*, 2007, **102**, 073510.
48 Z. Liu, W. Zhang, W. Gao and T. Mori, *Energy Environ. Sci.*, 2021, **14**, 3579–3587.
49 A. Bhui, M. Dutta, M. Mukherjee, K. S. Rana, A. K. Singh, A. Soni and K. Biswas, *Chem. Mater.*, 2021, **33**, 2993–3001.
50 M. Mukherjee and A. K. Singh, *ACS Appl. Mater. Interfaces*, 2020, **12**, 8280–8287.
51 Y. Luo, J. Wang, Y. Li and J. Wang, *Sci. Rep.*, 2016, **6**, 29801.
52 X. Yu, H. Shao, X. Wang, Y. Zhu, D. Fang and J. Hong, *J. Mater. Chem. A*, 2020, **8**, 3128–3134.
53 T. Pandey, A. S. Nissimagoudar, A. Mishra and A. K. Singh, *J. Mater. Chem. A*, 2020, **8**, 13812–13819.
54 Y. Shen, F. Q. Wang and Q. Wang, *Nano Energy*, 2020, **73**, 104822.
55 Y. Takagiwa and K. Kimura, *Sci. Technol. Adv. Mater.*, 2014, **15**, 044802.
56 Y. Yu, M. Cagnoni, O. Cojocaru-Mirédin and M. Wuttig, *Adv. Funct. Mater.*, 2020, **30**, 1904862.
57 X. Su, N. Zhao, S. Hao, C. C. Stoumpos, M. Liu, H. Chen, H. Xie, Q. Zhang, C. Wolverton, X. Tang and M. G. Kanatzidis, *Adv. Funct. Mater.*, 2019, **29**, 1806534.
58 H. Kageyama, K. Hayashi, K. Maeda, J. P. Attfield, Z. Hiroi, J. M. Rondinelli and K. R. Poeppelmeier, *Nat. Commun.*, 2018, **9**, 772.
59 Y. Pei, X. Shi, A. Lalonde, H. Wang, L. Chen and G. J. Snyder, *Nature*, 2011, **473**, 66–69.
60 Y. Pei, H. Wang and G. J. Snyder, *Adv. Mater.*, 2012, **24**, 6125–6135.
61 W. Liu, K. C. Lukas, K. McEnaney, S. Lee, Q. Zhang, C. P. Opeil, G. Chen and Z. Ren, *Energy Environ. Sci.*, 2013, **6**, 552–560.
62 L.-D. Zhao, J. He, D. Berardan, Y. Lin, J.-F. Li, C. Nan and N. Dragoe, *Energy Environ. Sci.*, 2014, **7**, 2900–2924.
63 G.-K. Ren, S. Wang, Z. Zhou, X. Li, J. Yang, W. Zhang, Y.-H. Lin, J. Yang and C.-W. Nan, *Nat. Commun.*, 2019, **10**, 2814.
64 J. Ding, B. Xu, Y. Lin, C. Nan and W. Liu, *New J. Phys.*, 2015, **17**, 083012.
65 J. M. Hodges, Y. Xia, C. D. Malliakas, T. J. Slade, C. Wolverton and M. G. Kanatzidis, *Chem. Mater.*, 2020, **32**, 10146–10154.
66 C. Doussier, P. Léone and Y. Moëlo, *Solid State Sci.*, 2004, **6**, 1387–1391.
67 C. Doussier, G. André, P. Léone, E. Janod and Y. Moëlo, *J. Solid State Chem.*, 2006, **179**, 486–491.
68 C. Doussier, Y. Moëlo and P. Léone, *Solid State Sci.*, 2006, **8**, 652–659.
69 K. Momma and F. Izumi, *J. Appl. Crystallogr.*, 2011, **44**, 1272–1276.
70 S. A. Sunshine and J. A. Ibers, *Acta Crystallogr. Sect. C Cryst. Struct. Commun.*, 1987, **43**, 1019–1022.
71 T. Tadano and S. Tsuneyuki, *Phys. Rev. B*, 2015, **92**, 054301.
72 M. Simoncelli, N. Marzari and F. Mauri, *Nat. Phys.*, 2019, **15**, 809–813.
73 W. Zhou, Y. Cheng, K. Chen, G. Xie, T. Wang and G. Zhang, *Adv. Funct. Mater.*, 2020, **30**, 1903829.
74 J. M. Ziman, *Electrons and phonons: the theory of transport phenomena in solids.*, Oxford University Press, Oxford, 2001.
75 L. Lindsay, *Nanoscale Microscale Thermophys. Eng.*, 2016, **20**, 67–84.
76 L. Lindsay, D. A. Broido, J. Carrete, N. Mingo and T. L. Reinecke, *Phys. Rev. B*, 2015, **91**, 121202.

77 C. Yuan, J. Li, L. Lindsay, D. Cherns, J. W. Pomeroy, S. Liu, J. H. Edgar and M. Kuball, *Commun. Phys.*, 2019, **2**, 43.
78 R. Wei, S. Song, K. Yang, Y. Cui, Y. Peng, X. Chen, X. Hu and X. Xu, *J. Appl. Phys.*, 2013, **113**, 053503.
79 H. R. Shanks, P. D. Maycock, P. H. Sidles and G. C. Danielson, *Phys. Rev.*, 1963, **130**, 1743–1748.
80 A. Jeżowski, B. A. Danilchenko, M. Boćkowski, I. Grzegory, S. Krukowski, T. Suski and T. Paszkiewicz, *Solid State Commun.*, 2003, **128**, 69–73.
81 H. Y. Chen, N. Savvides, T. Dasgupta, C. Stiewe and E. Mueller, *Phys. status solidi*, 2010, **207**, 2523–2531.
82 D. T. Morelli, T. Caillat, J.-P. Fleurial, A. Borshchevsky, J. Vandersande, B. Chen and C. Uher, *Phys. Rev. B*, 1995, **51**, 9622–9628.
83 C. B. Satterthwaite and R. W. Ure, *Phys. Rev.*, 1957, **108**, 1164–1170.
84 Z. Tian, J. Garg, K. Esfarjani, T. Shiga, J. Shiomi and G. Chen, *Phys. Rev. B*, 2012, **85**, 184303.
85 E. S. Toberer, A. F. May and G. J. Snyder, *Chem. Mater.*, 2010, **22**, 624–634.
86 T. Caillat, J.-P. Fleurial and A. Borshchevsky, *J. Phys. Chem. Solids*, 1997, **58**, 1119–1125.
87 L.-D. Zhao, S.-H. Lo, Y. Zhang, H. Sun, G. Tan, C. Uher, C. Wolverton, V. P. Dravid and M. G. Kanatzidis, *Nature*, 2014, **508**, 373–377.
88 K. Takahata, Y. Iguchi, D. Tanaka, T. Itoh and I. Terasaki, *Phys. Rev. B*, 2000, **61**, 12551–12555.
89 B. Koley, A. Lakshan, P. R. Raghuvanshi, C. Singh, A. Bhattacharya and P. P. Jana, *Angew. Chemie Int. Ed.*, 2021, **60**, 9106–9113.
90 P. Giannozzi, S. Baroni, N. Bonini, M. Calandra, R. Car, C. Cavazzoni, D. Ceresoli, G. L. Chiarotti, M. Cococcioni, I. Dabo, A. Dal Corso, S. de Gironcoli, S. Fabris, G. Fratesi, R. Gebauer, U. Gerstmann, C. Gougoussis, A. Kokalj, M. Lazzeri, L. Martin-Samos, N. Marzari, F. Mauri, R. Mazzarello, S. Paolini, A. Pasquarello, L. Paulatto, C. Sbraccia, S. Scandolo, G. Sclauzero, A. P. Seitsonen, A. Smogunov, P. Umari and R. M. Wentzcovitch, *J. Phys. Condens. Matter*, 2009, **21**, 395502.
91 P. Giannozzi, O. Andreussi, T. Brumme, O. Bunau, M. Buongiorno Nardelli, M. Calandra, R. Car, C. Cavazzoni, D. Ceresoli, M. Cococcioni, N. Colonna, I. Carnimeo, A. Dal Corso, S. de Gironcoli, P. Delugas, R. A. DiStasio, A. Ferretti, A. Floris, G. Fratesi, G. Fugallo, R. Gebauer, U. Gerstmann, F. Giustino, T. Gorni, J. Jia, M. Kawamura, H.-Y. Ko, A. Kokalj, E. Küçükbenli, M. Lazzeri, M. Marsili, N. Marzari, F. Mauri, N. L. Nguyen, H.-V. Nguyen, A. Otero-de-la-Roza, L. Paulatto, S. Poncé, D. Rocca, R. Sabatini, B. Santra, M. Schlipf, A. P. Seitsonen, A. Smogunov, I. Timrov, T. Thonhauser, P. Umari, N. Vast, X. Wu and S. Baroni, *J. Phys. Condens. Matter*, 2017, **29**, 465901.
92 P. E. Blöchl, *Phys. Rev. B*, 1994, **50**, 17953–17979.
93 G. Kresse and D. Joubert, *Phys. Rev. B*, 1999, **59**, 1758–1775.
94 G. I. Csonka, J. P. Perdew, A. Ruzsinszky, P. H. T. Philipsen, S. Lebègue, J. Paier, O. A. Vydrov and J. G. Ángyán, *Phys. Rev. B*, 2009, **79**, 155107.
95 T. Tadano, Y. Gohda and S. Tsuneyuki, *J. Phys. Condens. Matter*, 2014, **26**, 225402.